Supporting Information

Solvent-Assisted Self-Assembly of Metal-Organic Framework-Based Biocatalyst for Cascaded Reactions-Driven Photodynamic Therapy

Liangcan He,[†‡] Qianqian Ni,[‡] Jing Mu,[‡] Wenpei Fan,[*,⊥] Lu Liu,[§] Zhantong Wang,[‡] Ling Li,[‡] Wei Tang,[‡] Yijing Liu,[‡] Yaya Cheng,[‡] Longguang Tang,[‡] Zhen Yang,[‡] Yuan Liu,[‡] Jianhua Zou,[‡] Weijing Yang,[‡] Orit Jacobson,[‡] Fan Zhang,[§] Pintong Huang,[*,†] Xiaoyuan Chen[*,‡]

[†]Department of Ultrasound in Medicine, The Second Affiliated Hospital of Zhejiang University School of Medicine, Zhejiang 310009, P. R. China

[‡]Laboratory of Molecular Imaging and Nanomedicine, National Institute of Biomedical Imaging and Bioengineering, National Institutes of Health, Bethesda, MD, 20892, USA

[⊥]State Key Laboratory of Natural Medicines and Jiangsu Key Laboratory of Drug Discovery for Metabolic Diseases, Center of Advanced Pharmaceuticals and Biomaterials, China Pharmaceutical University, Nanjing, 210009, PR China

[§]Department of Chemistry, State Key Laboratory of Molecular Engineering of Polymers, Shanghai Key Laboratory of Molecular Catalysis and Innovative Materials and iChem, Fudan University, Shanghai 200433, P. R. China

Corresponding Authors: * shawn.chen@nih.gov, * huangpintong@zju.edu.cn, * wenpei.fan@cpu.edu.cn

Experimental Details

Materials:
All starting materials were obtained from commercial supplies. The salt crystal NH_4F, $YCl_3·6H_2O$, $YbCl_3·6H_2O$, $ErCl_3·6H_2O$, and other reagents NaOH, ethanol, cyclohexane, octadecene (ODE) (>90%), oleic acid (OA, >90%), Zirconium tetrachloride, 3,4-Dihydroxyhydrocinnamic acid (DHCA), O-Methyl-O'-succinylpolyethylene glycol 2000 (PEG-COOH), 1,3-diphenylisobenzofuran (DPBF) and *N,N*-dimethylformamide (DMF) were purchased from Sigma-Aldrich. Fe(III) meso-tetra(4-carboxyphenyl)porphine chloride (Fe-TCPP) and tetrakis(4-carboxyphenyl)porphine (TCPP) were purchased from VWR. All chemical reagents of analytical grade were used directly without further purification.

Cell lines and animals' model:
The U87MG human glioblastoma cell line was obtained from the American Type Culture Collection and cultured with Dulbecco's Modified Eagle Medium (DMEM) in the cell culture flask. Athymic nude mice were purchased from Envigo laboratories. The tumor model was established by subcutaneous injection of around 4×10^6 U87MG cells into the right hind limb of mice. All the experimental procedures were conducted following a protocol approved by the animal care and use committee (ACUC) of the National Institutes of Health Clinical Center (NIHCC).

Cytotoxicity Assay:
The cell viability of U87MG cells was determined by using the MTT assay. U87MG cells were seeded into a 96-well cell culture plate at 10^4 per well and incubated for 24 h at 37 ˚C under 5% CO_2. Then, pegylated modified UMOFs or UMOFs@Au NPs (all the samples are PEGylated in the following *in vitro* and *in vivo* experiments) dispersed in DMEM with varied concentrations (0, 6.25, 12.5, 25, 50, and 100 μg mL^{-1}) was added to each well. The cells were incubated for another 24 h at 37 ˚C under 5% CO_2. After incubation, the old media were removed, and the cell wells

were washed with PBS to remove the non-uptake particles, followed by addition of 90 μL of fresh media. Then 20 μL of filter-sterilized MTT reagent (5 mg mL^{-1} in PBS) was added into each well, and the plates were incubated at 37 ˚C. After further 4 h of incubation, the media was removed, and the precipitated formazan crystals were dissolved by adding DMSO. Absorption values of the dissolved formazan crystals in each well were measured at 570 using a microplate reader. All the samples were prepared in triplicate.

Photodynamic therapy assay:
U87MG cells were incubated with PBS, UMOFs and UMOFs@Au NPs at a final concentration of 10 μg mL^{-1} for 4 h. Excess nanoparticles were removed and washed with PBS, followed by addition of 100 μL of fresh media. Then 980 nm laser (1.0 W/cm^{-2}) was used to irradiate each cell well in the 96-well plate. After 10 min irradiation, the old media were then replaced with fresh culture media and cultivated for another 12 h at 37 °C. Cell viability was determined by MTT assay. All the samples were prepared in triplicate.

Measurement of absolute fluorescence quantum yield of UCNPs and related materials:
We have measured the upconversion quantum yield (UCQY) under 980 nm laser excitation (3 W/cm^2). Consistent with the literature[1], the UCQY for our core only UCNPs is low, with 0.32 ± 0.09% for the ~30 nm UCNPs. In contrast, the UCQY is greatly increased to 6.55 ± 0.34% for the ~29 nm core-shell-shell UCNPs structure due to reduced surface quenching.

Measurement of absolute fluorescence quantum yield of UCNPs and related materials in DMF: The fluorescence quantum yield is the probability of a sample emitting a photon through fluorescence when it is excited by a single photon. It is therefore also the percentage of photons emitted by a bulk sample when a given number of photons are absorbed by the sample, i.e. the number of photons emitted divided by the number of photons absorbed by a sample. The number of photons absorbed by a bulk sample is equal to the number of photons incident on the sample minus the photons passing through and not being absorbed by it.

The quantum yield can thus be calculated if the following three parameters are known:
1, number of photons incident on the sample volume;
2, number of photons not absorbed by the sample;
3, number of photons emitted by the sample.

$$\eta = \frac{\varepsilon}{\alpha} = \frac{\int L_{emission}}{\int E_{solvent} - \int E_{sample}}$$

Where ε is the photons emitted by the sample;
η is the quantum yield;
$L_{emission}$ is the luminescence emission spectrum of the sample, collected using the sphere;
E_{sample} is the spectrum of the light used to excite the sample, collected using the sphere;
$E_{solvent}$ is the spectrum of the light used for excitation with only the solvent in the sphere, collected using the sphere.

Singlet oxygen generation test:
The 980 nm laser was used for singlet oxygen generation tests. The irradiance of laser is 1 W/cm^2. Singlet oxygen sensor green (SOSG) reagent (Life Technologies, USA) was employed for the detection of singlet oxygen under dark and light irradiation in hypoxic or normoxic conditions, respectively.

Singlet oxygen generation test under normoxic condition: SOSG was employed for detecting singlet oxygen. 2 μL of SOSG DMSO solution (5×10^{-3} M) was added into 1 mL of MOFs@Au or UMOFs@Au NPs buffer solution. The samples then were irradiated with 980 nm laser light for 0, 5, 10, 15, 20, 25 and 30 min. Every 5 min, 100 μL of solution was taken out and the fluorescence intensity was obtained on a fluorimeter.

Singlet oxygen generation test under hypoxic condition: UMOFs@Au NPs were dispersed in buffer solution. SOSG stock solution and H_2O_2 was added to afford a final SOSG concentration of 12.5 μM and H_2O_2 concentration of 100 μM. Another control group was prepared by adding only SOSG stock solution to the suspension without H_2O_2. Oxygen was then removed from these mixture samples by nitrogen (N_2) bubbling for 20 min. These mixtures were subsequently exposed to 980 nm laser irradiation for 0, 5, 10, 15, 20, 25 and 30 min. The fluorescence at different time points was measured by a fluorimeter.

Singlet oxygen generation test in U87MG cells: U87MG cells were seeded on cover slides in 8-well detachable plate at 5×10^4 cells per well and further cultured for 24 h. Then the following treatments were done: (1) PBS, (2) laser, (3) UMOFs, (4) UMOFs@Au, (5) UMOFs with laser irradiation, (6) UMOFs@Au with laser irradiation. UMOFs and UMOFs@Au NPs were added to the cells at the concentration of 10 μg/mL. SOSG was added 15 min before light irradiation. After incubation of 4 hours, cells were irradiated by the laser. The slides were then washed with PBS and observed under CLSM.

The singlet oxygen quantum yields of Fe-porphyrin MOFs and the hybrid system:

In order to quantify the quantum yields of the MOFs and MOFs-based hybrid system, the 1,3-diphenylisobenzofuran (DPBF) is used as the singlet oxygen ($^1O_2$) indicator to evaluate the $^1O_2$ generation. The $^1O_2$ quantum yield (φ_Δ) is calculated through monitoring the oxidation of DPBF with a UV-vis spectrophotometer. Herein, the relative quantum yield is determined by a standard method. For this, methylene blue (MB, $\varphi_{\Delta(std)} = 0.52$) is used as the standard to determine the $^1O_2$ quantum yields.[2,3] As both of the MB and porphyrin MOFs exhibit absorption around 660 nm, 660 nm LED light is used for the tests. Briefly, an oxygen-saturated solution of UMOFs, UMOFs@Au and MB individually containing 60 μM DPBF was prepared (in the dark) and irradiation with 660 nm LED light (60 mW/cm^2). The absorption of DPBF was monitored at different time points. And the quantum yields were calculated by the following equation.

$$\varphi_\Delta = \varphi_{\Delta(std)} \times \frac{S_x}{S_{std}} \times \frac{F_{std}}{F_x}$$

x: the sample;

std: MB;

S: slope of the absorbance of DPBF (418 nm) *vs* irradiation time;

F: absorption correction factor, F=1 - 10^{-OD} (OD: the optical density of the sample and MB at 660 nm)

Oxygen generation measurements:

The oxygen concentrations in PBS buffer solution was recorded in real time by tris(4,7-diphenyl-1,10-phenanthroline) ruthenium (II) dichloride complex ($Rn(dpp)_3 \cdot Cl_2$) in a sealed and N_2 bubbled cuvette. A fixed amount of H_2O_2 was added into the above solution to make the H_2O_2 final concentration at 150 μM and 2 mM, respectively. For 150 μM H_2O_2 solution, the UMOFs@Au NPs concentration was 1.3 μg/mL. Immediately after the addition of biocatalysts, the generated O_2 concentration was monitored by a fluorometer at 0, 1, 2, 3, 4, 5 and 6 min.

Flow cytometry of cellular uptake and confocal fluorescence imaging study:
The cellular uptake of UMOFs@Au NPs was evaluated in U87MG cells. The UMOFs@Au NPs were modified with N_α,N_α-bis(carboxymethyl)-L-lysine hydrate at 1:1 ratio (Fe-TCPP:ligand) and then conjugated with fluorescein isothiocyanate isomer I (FITC). The FITC modified NPs were redispersed for the cell uptake study. Cells were seeded in a 12-well plate at 3×10^5 cells per well and further cultured for 12 h. FITC conjugated NPs were added to the wells at a final concentration of 10 μg/mL. After incubation for 0.5, 1 and 2 h, the medium was removed, and the cells were washed with PBS. The redispersed cell solutions were used for the flow cytometry studies. For the confocal fluorescence imaging test, the FITC conjugated NPs (10 μg/mL) were added into the cells which were seeded in 8-well detachable chambers. After incubation for 0.5, 1 and 2 h, the medium was removed, and the cells were washed with PBS. The slides were then mounted with mounting medium with DAPI and were observed under a Zeiss LSM 780 confocal microscope.

Hypoxia treatment:
Briefly, U87MG cells were seeded in a 6-well plate at 4×10^5 cells per well on the day before treatment. The media were then exchanged for fresh medium and placed in an anaerobic chamber filled with 94% N_2, 5% CO_2 and 1% O_2 to induce hypoxia. The control cells were incubated in a normoxic condition containing 5% CO_2, 21% O_2.

Intracellular H_2O_2 assay:
Intracellular H_2O_2 was detected by using a hydrogen peroxide assay kit (Abcam). For hypoxic condition, cells were cultured in the hypoxic chamber for 12 h and further incubated with PBS, AuNPs, UMOFs, or UMOFs@Au at a final concentration of 10 μg/mL for 4 h. Then the medium was replaced by assay buffer and incubated for another 1 h. After washing with PBS, intracellular H_2O_2 was observed under a Zeiss LSM 780 confocal microscope.
For the normoxic condition, cells were treated with 100 μM H_2O_2 for 12 h and then further incubated with PBS, AuNPs, UMOFs, or UMOFs@Au at a final concentration of 10 μg/mL for 4 h. The medium was replaced with assay buffer and incubated for another 1 h. After washing with PBS, intracellular H_2O_2 was observed under a Zeiss LSM 780 confocal microscope.

PET labeling and *in Vivo* PET imaging:
For the ^{64}Cu labeling, the following procedure was used. 2 μL of $^{64}CuCl_2$ (pH 1-2) was added to a solution containing 1.5 mg sodium ascorbate in 40 μL 1M borate buffer pH 8. The mixture was shortly vortexed and incubate for 3 min at room temperature. Then, 200 μL of UMOF@Au NPs (0.5 mg/mL) in 18.2 Ω water were added. The reaction was agitated for 0.5 h at 37 °C. Radiochemical purity was determined using iTLC plates, developed in 0.1 M citric acid pH 5 (*Rf* of ^{64}Cu-UMOFs@Au NPs ~ 0.1, *Rf* of uncomplexed ^{64}Cu ~ 0.9).
The ^{64}Cu-labeled UMOFs@Au NPs were systematically administrated into U87MG tumor-bearing mice at around 100 μCi. The PET images were collected on a micro Inveon PET scanner at 1, 4, 24, and 48 h p.i. Regions of interest (ROIs) were circled, and the corresponding radioactivities were quantified on the areas of tumors, spleens and livers in the decay-corrected whole-body coronal images.

***In Vivo* anticancer effect:**

When the tumor size reached 80-100 mm^3, U87MG tumor bearing mice were randomly divided into five groups and treated with various formulations: (1) PBS, (2) laser, (3) UMOFs, (4) UMOFs@Au, (5) UMOFs with laser irradiation, (6) UMOFs@Au with laser irradiation. UMOFs and UMOFs@Au NPs were injected intravenously at a concentration of 1.5 mg/mL. In the experiments, the 980 nm laser (0.7 W/cm^2, 20 min, 1 min break after 1 min irradiation) was used for the irradiation of tumors at 24 h post-injection. Two days later, another injection and treatment were applied with the same parameters. The tumor sizes were measured with a caliper every two days and calculated by the formula (width × width × length)/2. Body weight of each mice was monitored every two days. Tumors and major organs were sectioned for hematoxylin-eosin staining (H&E) and immunofluorescence analyses.

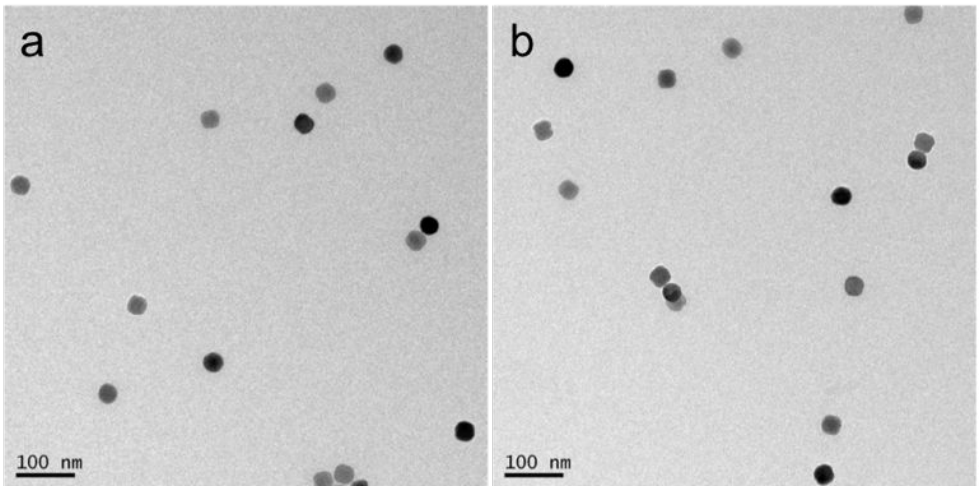

Figure S1. TEM images of the UCNPs before (a) and after (b) the carboxylic acid (DHCA) modification.

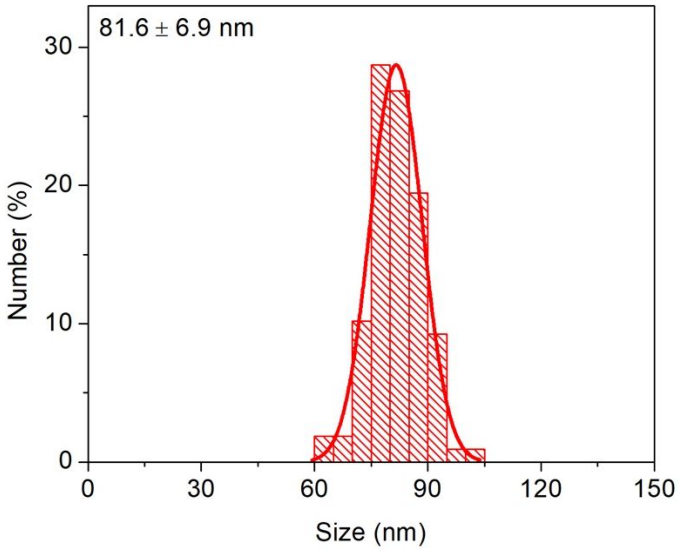

Figure S2. Particle size distribution of the UMOFs NPs.

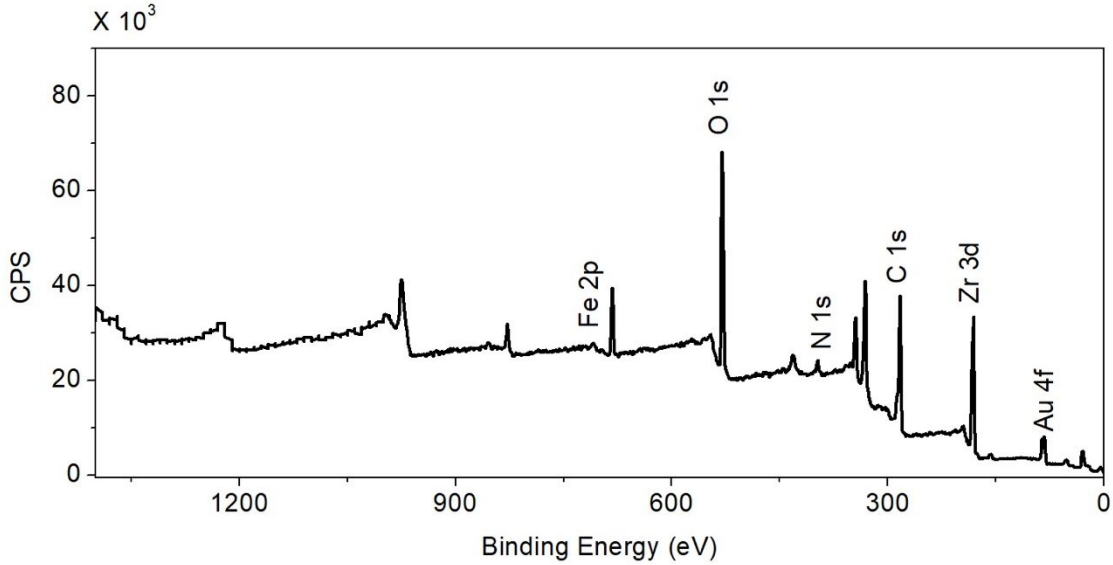

Figure S3. XPS spectrum of UMOFs@Au NPs. Based on the XPS spectrum, it was found the surface atom ratio of UMOFs@Au was Fe: Au: N: Zr = 1: 1.08: 4.21: 10.95.

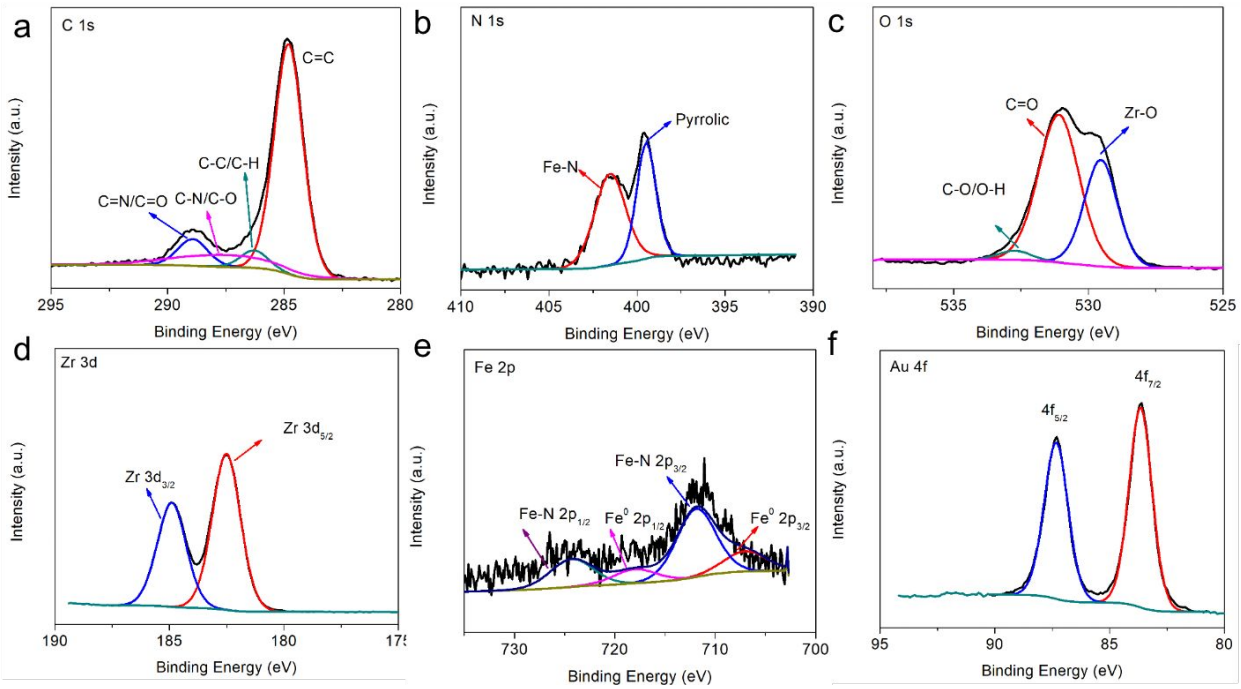

Figure S4. High-resolution XPS spectra of (a) C 1s, (b) N 1s, (c) O 1s, (d) Zr (3d), (e) Fe 2p and (f) Au 4f.

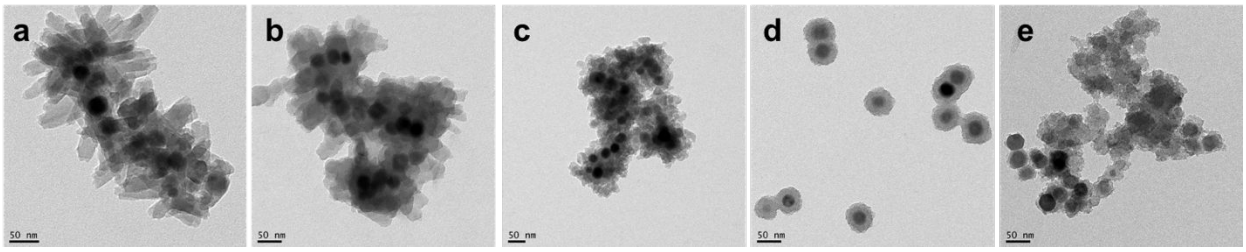

Figure S5. Effect of the ethanol ratio on the synthesis of core-shell UMOFs nanoparticles: (a) 16.7%, (b) 25%, (c) 33.3%, (d) 50% and (e) 100%.

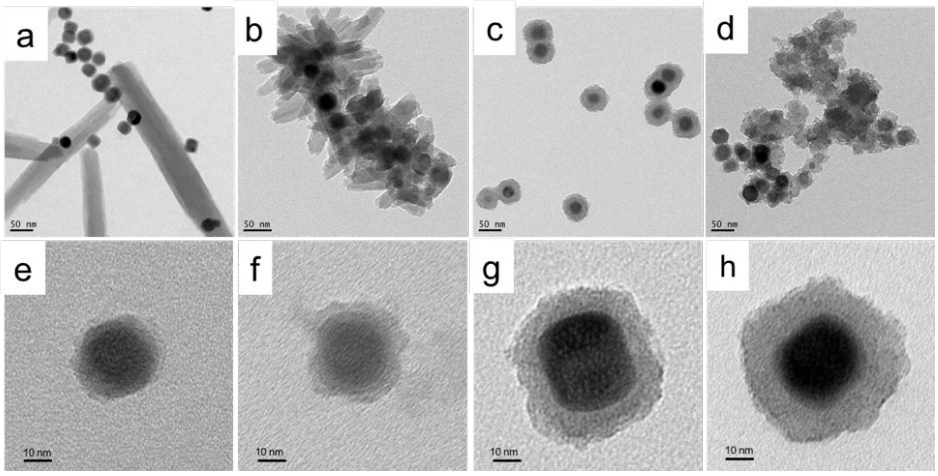

Figure S6. TEM images of UCNPs/MOFs hybrid structures synthesized in: (a) DMF solution, (b) DMF/ethanol (5/1) solution, (c) DMF/ethanol (1/1) solution, (d) ethanol solution. TEM images of the core-shell UMOFs NPs obtained at different reaction time: (e) 5 min, (f) 20 min, (g) 60 min, and (h) 120 min.

The nucleation of one MOF on the existing topologically distinct UCNP surface is a heterogeneous nucleation process. According to the classic nucleation theory, the critical energy barrier of a heterogeneous nucleation process is equal to the product of the homogeneous nucleation energy barrier and a function of the contact angle (θ).[4-6]

$$\Delta G_{heterogeneous} = \Delta G_{homogeneous} \times \frac{2 - 3cos\theta + cos^3\theta}{4} \ (0 \leqslant \theta < 180^o)$$

The formation of UMOFs core-shell nanostructures depends on two factors: (1) the nucleation kinetics, (2) the surface properties of the UCNP cores. Due to the mismatched unit cell parameters of MOFs and UCNPs, the UCNPs core surface was modified with “nucleation friendly” 3,4-dihydroxyhydrocinnamic acid (DHCA) molecules to lower the nucleation energy barrier.[7,8] On the other hand, the MOF precursors concentrations also affect the nucleation kinetics.[9] The higher concentration would result in lower critical nucleation energy barrier, which promoted the formation of a large number of nuclei. For a given concentration of solute, a larger number of nuclei mean smaller sized nuclei (Figure S4).

In this work, the DMF is the solvent of metal and ligand, which could control the extent of deprotonation of the carboxylate ligands. The DMF could be converted into its corresponding amines at higher temperatures and thus lead to deprotonation of carboxylates. The addition of ethanol affects the bridging modes of ligand and polarity of the solvent medium. Herein, the ethanol acts as a structure directing agent for the crystal growth process, which directly or indirectly influences the coordination behavior of metal and ligand regulates the formation of coordination environment in the assembly process. Therefore, the reaction medium affects the morphology of MOFs crystals.[10] Based on the

TEM results and the above discussion, the possible mechanism for MOFs formation around UCNPs and property modulation in DMF/ethanol mixtures is proposed in the following.

(1) With no ethanol in the system, the coordination environment of the MOFs has no change. The rod-shape MOFs products were formed by coordination chelation between Fe-TCPP ligand and Zr_6 clusters. Due to the mismatched unit cell parameters between the MOFs and UCNPs, very low ratio of core-shell UMOFs structures are formed in this process. Conversely, the MOFs have the tendency towards anisotropic growth to minimize the surface energy, resulting in large sized MOFs products.

(2) When a little amount of ethanol (~16.7%) was added to the reaction mixture, the crystal growth and size of the MOFs products could be effectively regulated with the assistance of nucleation modulator ethanol. The presence of ethanol could change the coordination environment of Zr_6 clusters, so the MOFs nucleate preferentially around the “nucleation friendly” DHCA molecules modified UCNPs cores instead of self-nucleation in the solution. Moreover, the anisotropic growth of MOF was also partially impeded, and small sized MOFs crystals with rough surface were synthesized.

(3) With a proper amount of ethanol (~50.0%) added into the system, the presence of ethanol largely influences the coordination behavior of Zr_6 clusters and the ligand Fe-TCPP. And it acts as a structure’s agent for the MOFs crystal growth process. In this case, the coordination chelation of Fe-TCPP with Zr_6 clusters is thus greatly facilitated around the “nucleation friendly” 3,4-dihydroxyhydrocinnamic acid (DHCA) molecules modified UCNPs cores, resulting in core-shell UMOFs structures with regular shape.

(4) With the ethanol amount reaching 100%, the intrinsic poor soluble property of TCPP-Fe molecules in ethanol causes them to easily aggregate into a cluster state, resulting in Zr-TCPP products with an irregular shape.

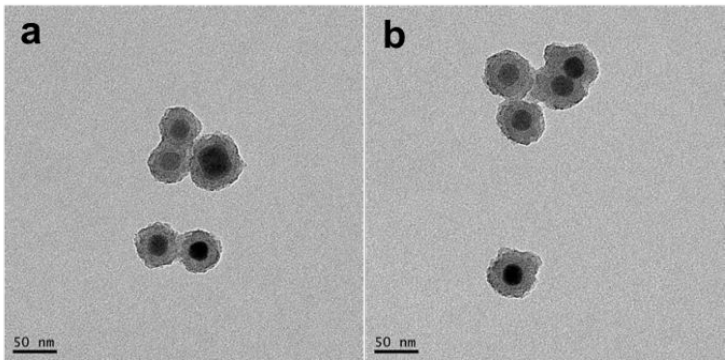

Figure S7. TEM images of UMOFs using carboxylic acid modified UCNPs seeds treated with (a) and without (b) NaOH solution.

In the ligand exchange of UCNPs, the pH change of the solution was not very necessary. The core-shell UMOFs could be synthesized at very high yield using carboxylic acid modified UCNPs seeds, which was treated with or without NaOH solution.

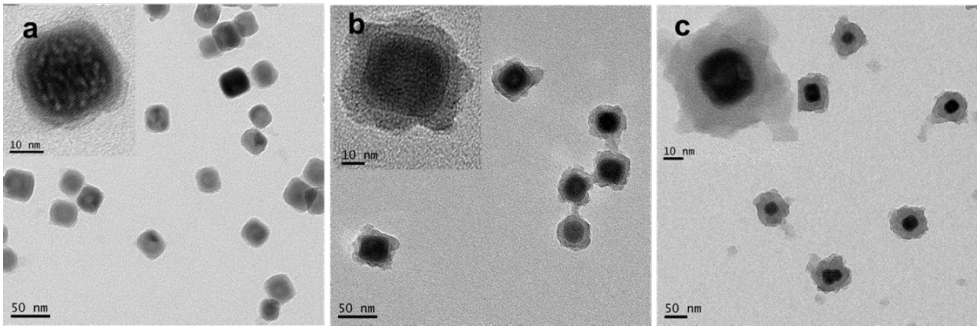

Figure S8. TEM images of core-shell UMOFs with different shell thicknesses: (a) ~2.7 nm, (b) ~8.3 nm, (c) ~23.5 nm.

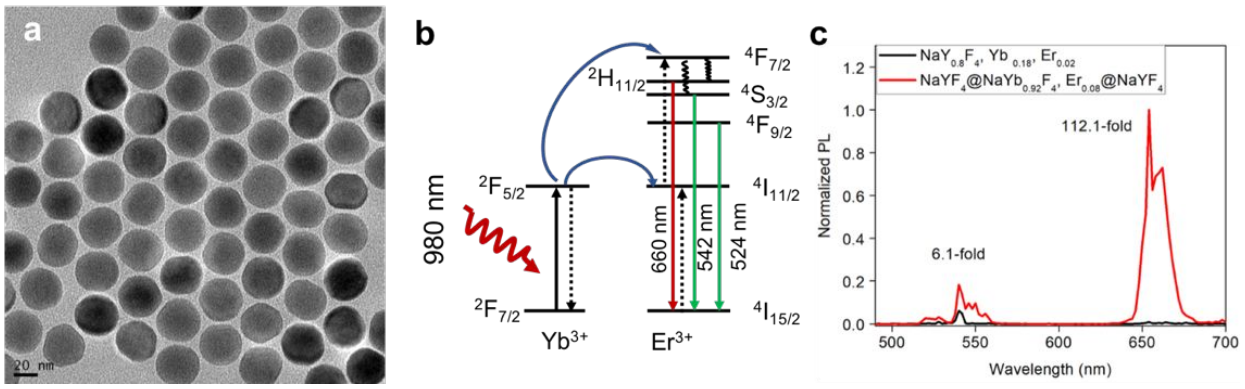

Figure S9. TEM image of (a) ~30 nm β-$NaY_{0.78}F_4$:$Yb_{0.2}$, $Er_{0.02}$. (b) Schematic illustration of the energy-transfer mechanism for the core-shell-shell β-$NaYF_4$@$NaYb_{0.92}F_4$:$Er_{0.08}$@$NaYF_4$ UCNPs with excitation multicolor UCL. (c) UCL spectra of the β-$NaYF_4$@$NaYb_{0.92}F_4$:$Er_{0.08}$@$NaYF_4$ and β-$NaY_{0.78}F_4$:$Yb_{0.2}$,$Er_{0.02}$ solution at the same concentration.

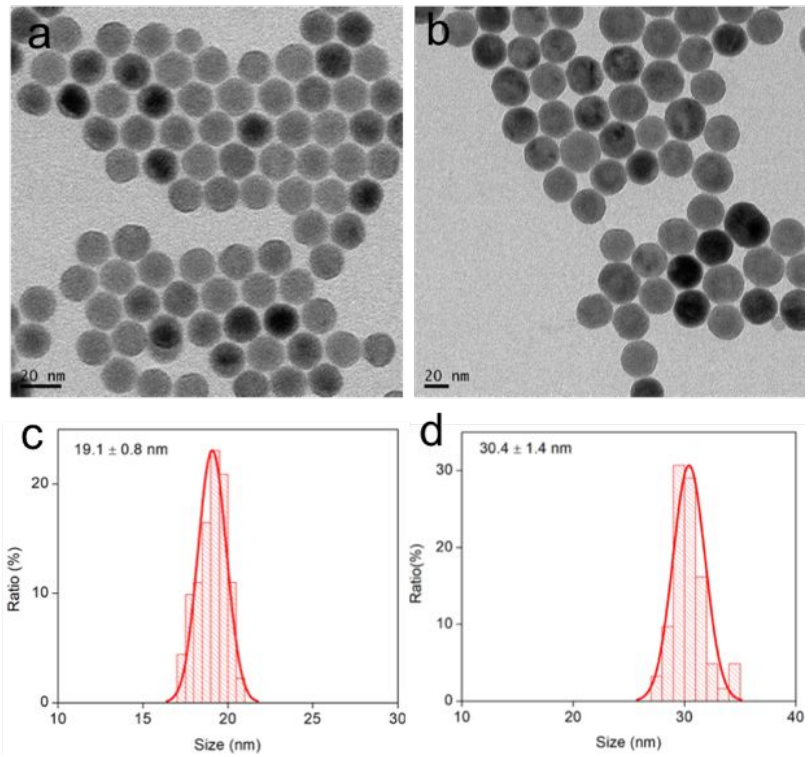

Figure S10. TEM image and size distribution of (a, c) $NaYF_4$:Yb,Er and (b, d) $NaYF_4$:Yb,Er@$NaYF_4$. The quantum yield of the core-shell UCNPs is around ~4.1% and ~1.7% in DMF and water, respectively.

Table S1. Summary of the UCNPs quantum yield.

Nanoparticle type	UCNP Type	UCNP size (nm)	Laser power (W/cm^2)	Upconversion quantum yield	Reference
bulk powder	$NaYF_4$, Yb/Er	>>100	20	3.0%	1
core	$NaYF_4$:Yb,Er	~15	4	0.3%	11
core-shell	$NaYF_4$:Yb/Tm @$NaYF_4$	43	0.027-130	1.2	12
core-shell	$NaYF_4$:Yb/Er/Nd @$NaYF_4$:Nd	40	80	0.22%	13
dye-sensitized core-shell	$NaYF_4$: Yb, Er@$NaYF_4$,Yb-IR806	~35	2 (800 nm laser)	5%	14
core-shell-shell	$NaYF_4$:Yb,Tm,Ca@ $NaYbF_4$:Ca@ $NaNdF_4$:Gd,Ca	10	7.5	0.4%	15
core-shell	$NaYF_4$:Yb/Er@ $NaYF_4$	38	2	1.8%	16
core-shell	$NaErF_4$@$NaYF_4$	19.7	2	0.17%	16
core-shell	$NaGdF_4$:Yb/Er@ $NaGdF_4$	19 x 8	3.0	0.2%	17
core-shell	$NaYF_4$:Tm@ $NaGdF_4$	8.4-11.3	1000	0.0027%-1.2%	18
core-shell	$NaYF_4$:Tm@ $NaGdF_4$	8.4-11.3	100000	0.1%-20%	18
core-shell	$NaYF_4$:Tm@ $NaGdF_4$	8.4-11.3	1000000	0.59%-20%	18
core- shell	$NaYbF_4$:Er @$NaYF_4$	~29	120	5.0%	19
core-shell-shell	$NaYF_4$@$NaYbF_4$:Er @$NaYF_4$	~29	120	5.4%	19
dye-sensitized core-shell	$NaYF_4$:Yb,Er@ $NaYF_4$:Nd,Yb/ICG	33	8	9.2% relative quantum yield	20, 21
UCNPs shell	PDA@UCNP-PEG/ Ce6	--	--	0.03%	22
core-shell	$NaYF_4$:Yb, Er@ $NaYF_4$	38	--	0.12%	23, 24
dye coated UCNPs	$NaYGdLuF_4$:Yb,Er	10.9-25.1	15-50	<0.01% water	25
core	$NaYF_4$:Yb,Er	~30	3	~0.32% and ~0.007% (water)	This work
core-shell	$NaYbF_4$:Er	~30	3	~4.1%	This work

	@$NaYF_4$			and ~1.7% (water)	
core-shell-shell	$NaYF_4$@ $NaYbF_4$:Er @$NaYF_4$	29.8 ± 2.2	3	~6.6 % and ~5.2 % (water)	This work
core-shell-shell	$NaYF_4$@ $NaYbF_4$:Er @$NaYF_4$	29.8 ± 2.2	30	~31.5 % and ~18.3 % (water)	This work

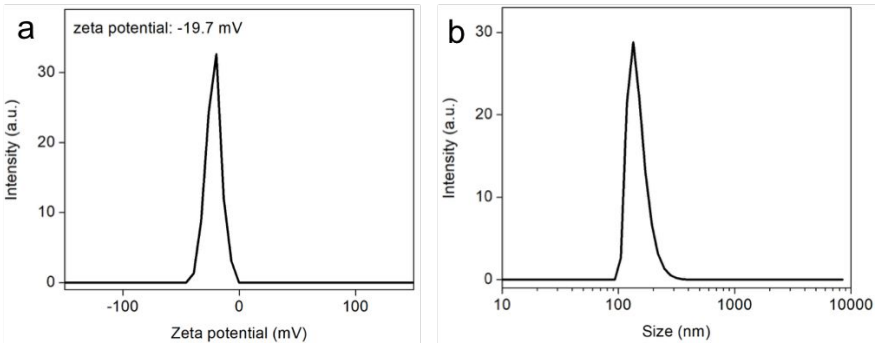

Figure S11. (a) Zeta potential of the UMOFs@Au NPs in aqueous solution. (b) Dynamic light scattering (DLS) of UMOFs@Au NPs in aqueous solution (~126.4 nm).

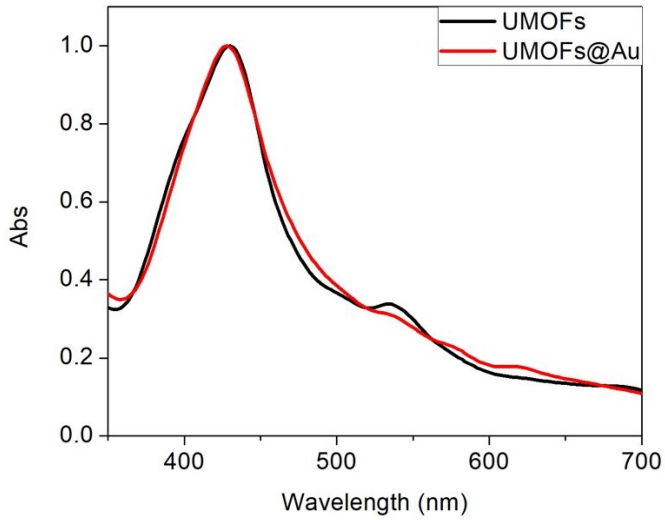

Figure S12. Normalized UV-vis absorption spectra of UMOFs and UMOFs@Au NPs.

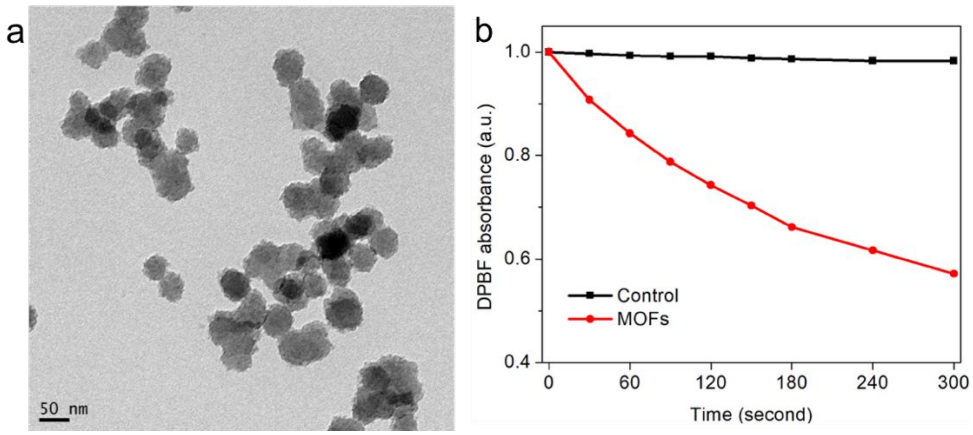

Figure S13. (a) TEM image of MOFs (the same method for the synthesis of UMOFs). (b) Relative absorbance of DPBF at 418 nm in different solutions exposed for 5 min under a 660 nm LED light (60 mW/cm^2).

Table S2. Quantitative analysis of the photoluminescence spectra of UMOFs and UMOFs@Au NPs.

	UCNPs	UMOFs	UMOFs@Au	MOFs
green emission	100%	53.1%	21.1%	--
absorbed green emission	--	46.9%	78.9%	--
red emission	100%	53.9%	45.6%	--
absorbed red emission	--	46.1%	54.4%	--

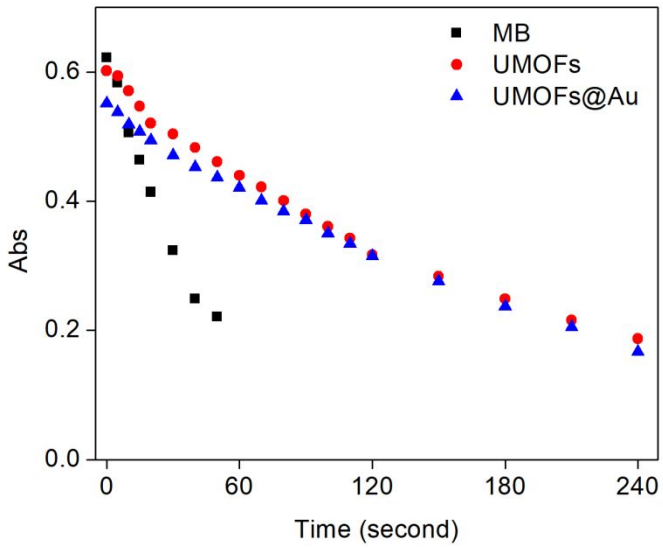

Figure S14. The singlet oxygen ($^1O_2$) quantum yields of Fe-porphyrin MOFs and the hybrid system.

The quantum yields were calculated by the following equation.

$$\varphi_{\Delta} = \varphi_{\Delta(\text{std})} \times \frac{S_x}{S_{std}} \times \frac{F_{std}}{F_x}$$

x: the sample;
std: MB;
S: slope of the absorbance of DPBF (418 nm) *vs* irradiation time;
F: absorption correction factor, F=1 - 10^{-OD} (OD: the optical density of the sample and MB at 660 nm)

Based on the above formula, the quantum yield is calculated as $\varphi_{\Delta\ (\text{UMOFs})}$ = 0.39, $\varphi_{\Delta\ (\text{UMOFs@Au})}$ = 0.36.

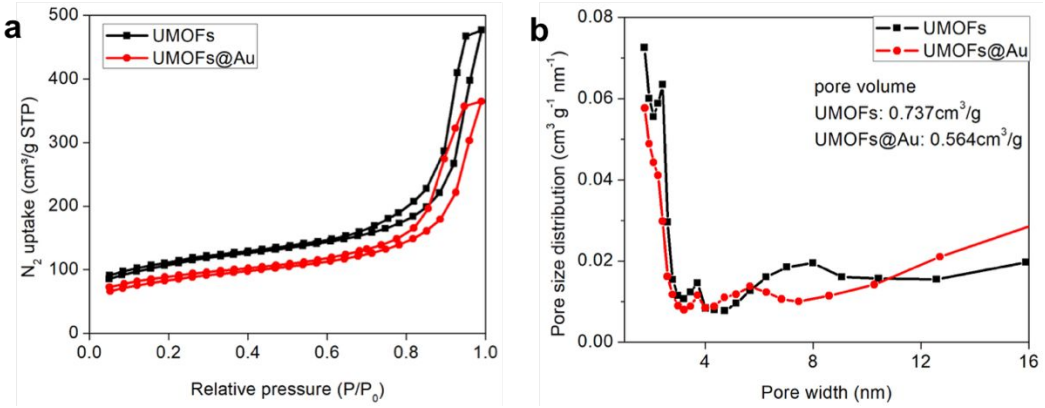

Figure S15. (a) N_2 adsorption-desorption isotherms of the core-shell UMOFs and UMOFs@Au NPs. b) Pore size distributions of the core-shell UMOFs and UMOFs@Au NPs.

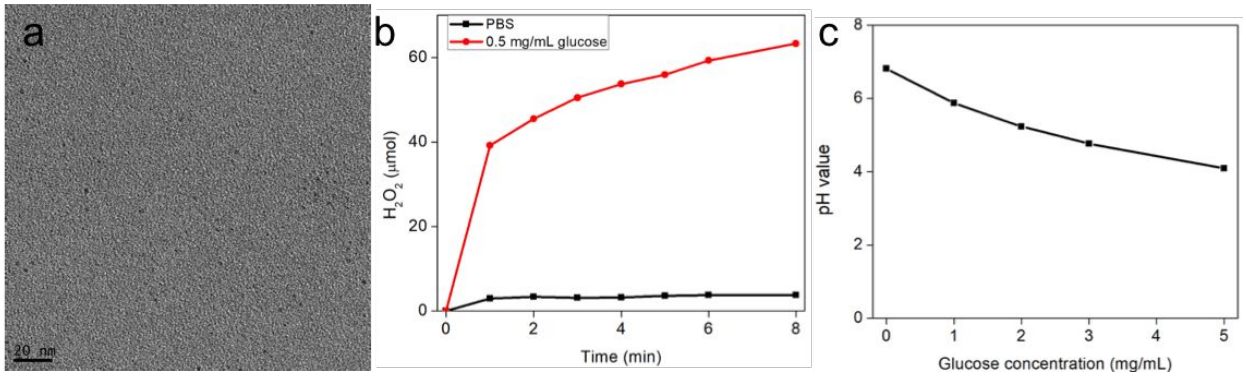

Figure S16. (a) TEM image of ultrasmall AuNPs (~2 nm). (b) Time-dependent H_2O_2 generation from ultrasmall Au NPs (equivalent to 10 μg/mL UMOFs@Au NPs in 0.5 mg/mL glucose solution, 10 min incubation). (c) The pH values of the glucose solution in the presence of UMOFs@Au NPs. The ultrasmall AuNPs could decompose the glucose and produced H_2O_2 and gluconic acid, resulting in lower pH values.

The ultrasmall Au NPs were synthesized by reducing $HAuCl_4$ solution (10 mL, 1 mM) with fresh prepared $NaBH_4$ (1 mL, 100 mM) in the presence of 111.1 mg PVP.

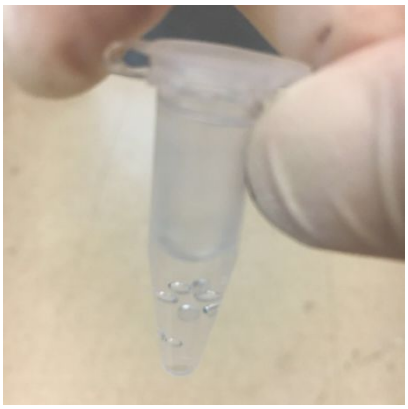

Figure S17. O_2 bubble was produced from the UMOFs@Au NPs solution (10 μg/mL) in the presence of H_2O_2 (150 μM). The appearance of bubble in the solution showed the highly catalytic activity of UMOFs@Au NPs in the production of O_2.

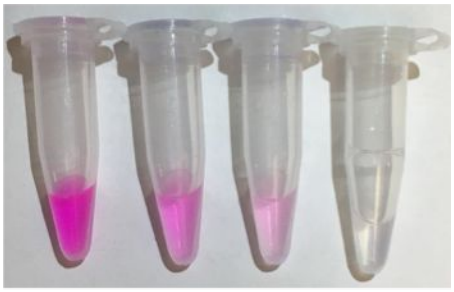

Figure S18. The glucose solution color (0.5 mg/mL, 100 μL) changes after adding 1 μL Hydrogen Peroxide Assay Kit and different volume of UMOFs@Au NPs (1) 0 μL, (2) 0.5 μL, (3) 1.0 μL and (4) 2.0 μL (equivalent to 10 μg/mL UMOFs@Au NPs in 0.5 mg/mL glucose solution, 10 min incubation).

The solution color changes further demonstrated that the increasing production of H_2O_2 with increasing of UMOFs@Au NPs.

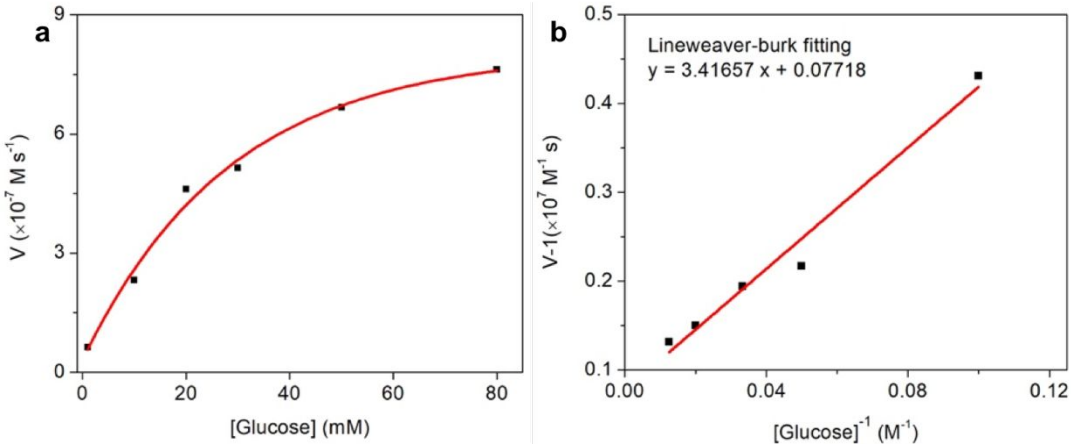

Figure S19. (a) Michaelis-Menten kinetics curve and (b) Lineweaver-Burk plotting of ultrasmall AuNPs.

In order to investigate the reaction rate of AuNPs in the glucose oxidation reaction, the catalytic performance of the UMOFs@Au was evaluated based on the Michaelis-Menten steady-state enzyme kinetic assay.[26] A series of glucose solutions were applied as the substrates. The maximum was calculated to be 12.96 × 10^{-7} M s^{-1} according to the Lineweaver-Burk plot.

To explore the impact of pH value on the enzyme-like activities of ultrasmall AuNPs, the hydrogen peroxide assay kit (ab102500, abcam company) is used to monitor the enzyme-mimic activity of ultrasmall AuNPs. The absorbance at 570 nm is plotted over time. Briefly, 5 μL of UMOFs@Au (1 mg/mL) is incubated with 200 μL of buffer solution with different pH values (pH = 4.5, 5.5, 6.5, 7.4 and 8.0), which contained HRP, OxiRed Probe and glucose substrate (Abcam company). The absorption at 570 nm was monitored over time. As shown in Figure S16, the ultrasmall AuNPs demonstrated a slightly higher catalytic activity at lower pH values.

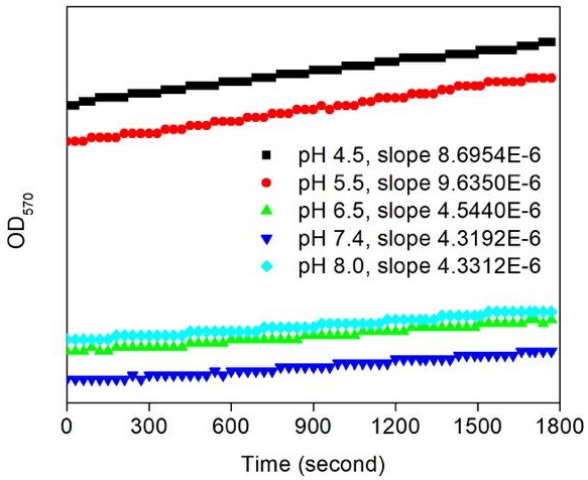

Figure S20. The effect of the pH value on the ultrasmall AuNPs GOx-mimic reactions.

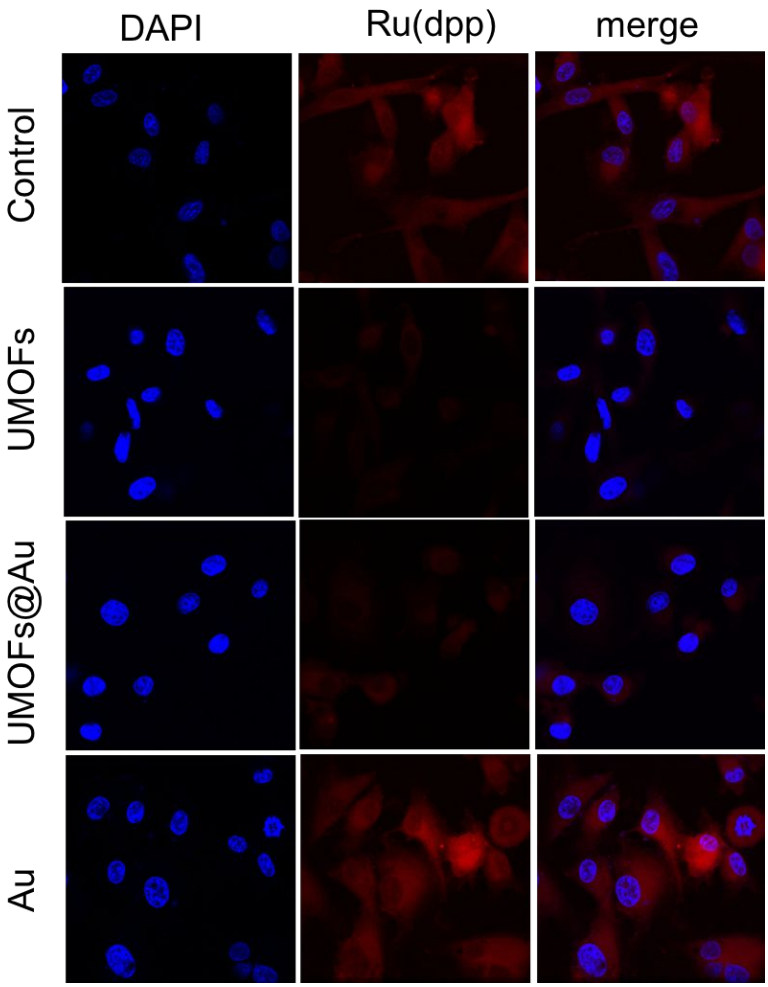

Figure S21. CLSM images of intracellular oxygen detection under hypoxic condition.

The presence of increased level of O_2 in the CLSM image of UMOFs@Au NPs demonstrating the balanced catalytic activities of the ultrasmall AuNPs and iron-MOFs in the tumor cells.

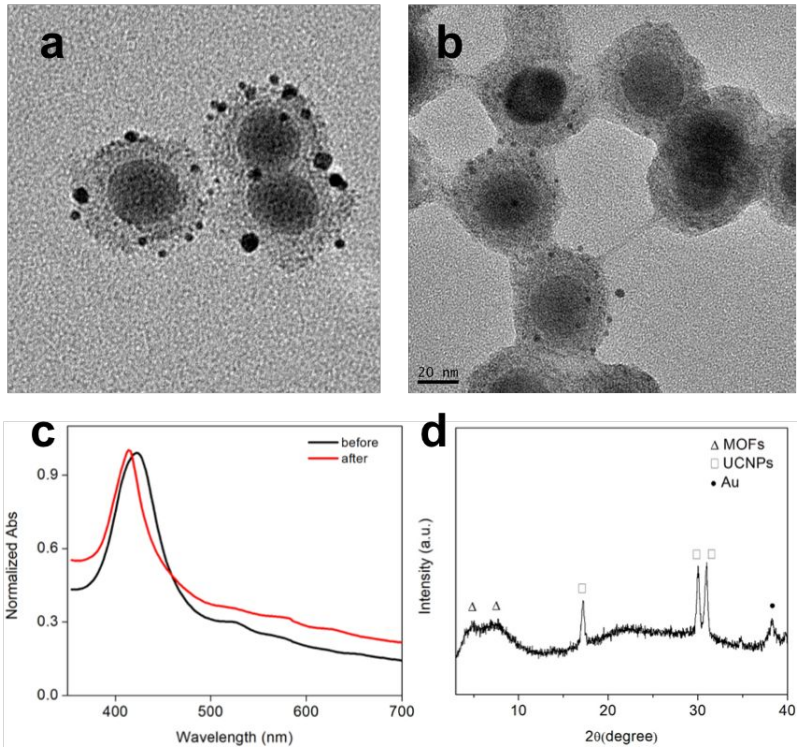

Figure S22. (a) TEM images of UMOFs@Au NPs before and (b) after immersing in DMEM for 24 h. (c) UV-vis spectra of UMOFs@Au NPs before and after immersing in DMEM for 24h. (d) XRD pattern of UMOFs@Au NPs cultured in DMEM for 24h.

The stability of the MOFs was characterized by TEM, UV-vis and XRD. As shown in Figure S17, there are little morphology changes for the UMOFs@Au NPs after dispersing in DMEM (with 10% FBS) for 24 h. Moreover, the UV-vis spectra indicated that there was slightly blue shift for UMOFs@Au NPs after immersing in DMEM (10% FBS) for 24 h. After immersing in DMEM (with 10% FBS) for 24 h, the UMOFs@Au NPs still maintained the crystal structures demonstrating good stability. In addition, it was found that the integrity of the UMOFs@Au NPs had little changes from the TEM images.

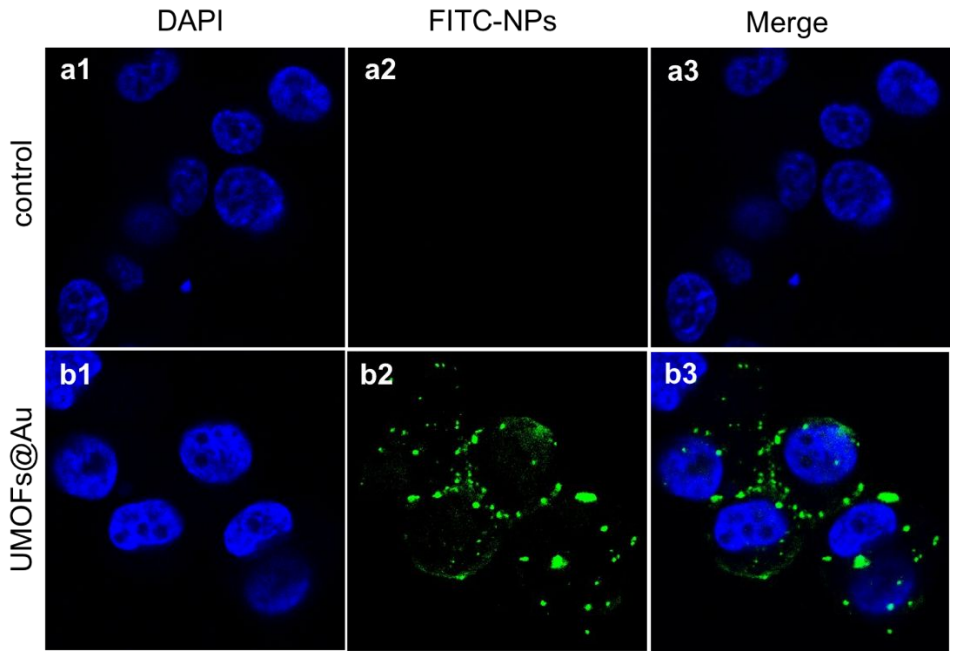

Figure S23. Confocal fluorescence images of the FITC labelled UMOFs@Au NPs cultured cells at 2h time point.

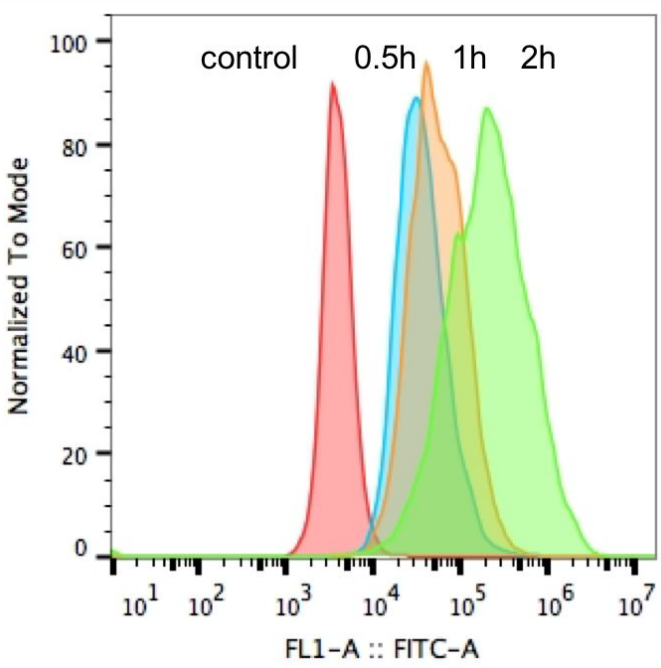

Figure S24. Flow cytometry analysis of cellular internalization of UMOFs@Au NPs in U87MG cells at different time points (NPs were modified with FITC).

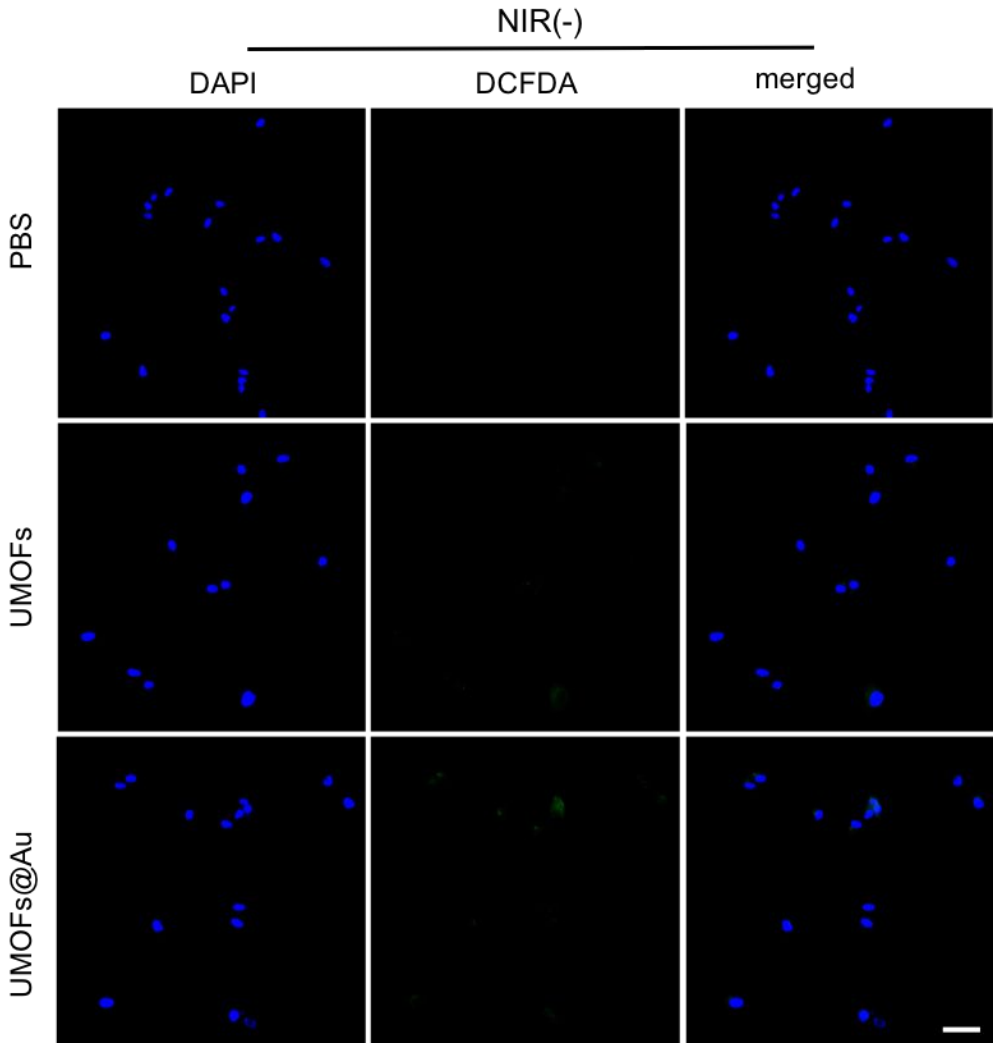

Figure S25. CLSM images of intracellular ROS generation by DCFDA assay. Six group experiments were conducted, without 980 nm laser irradiation.

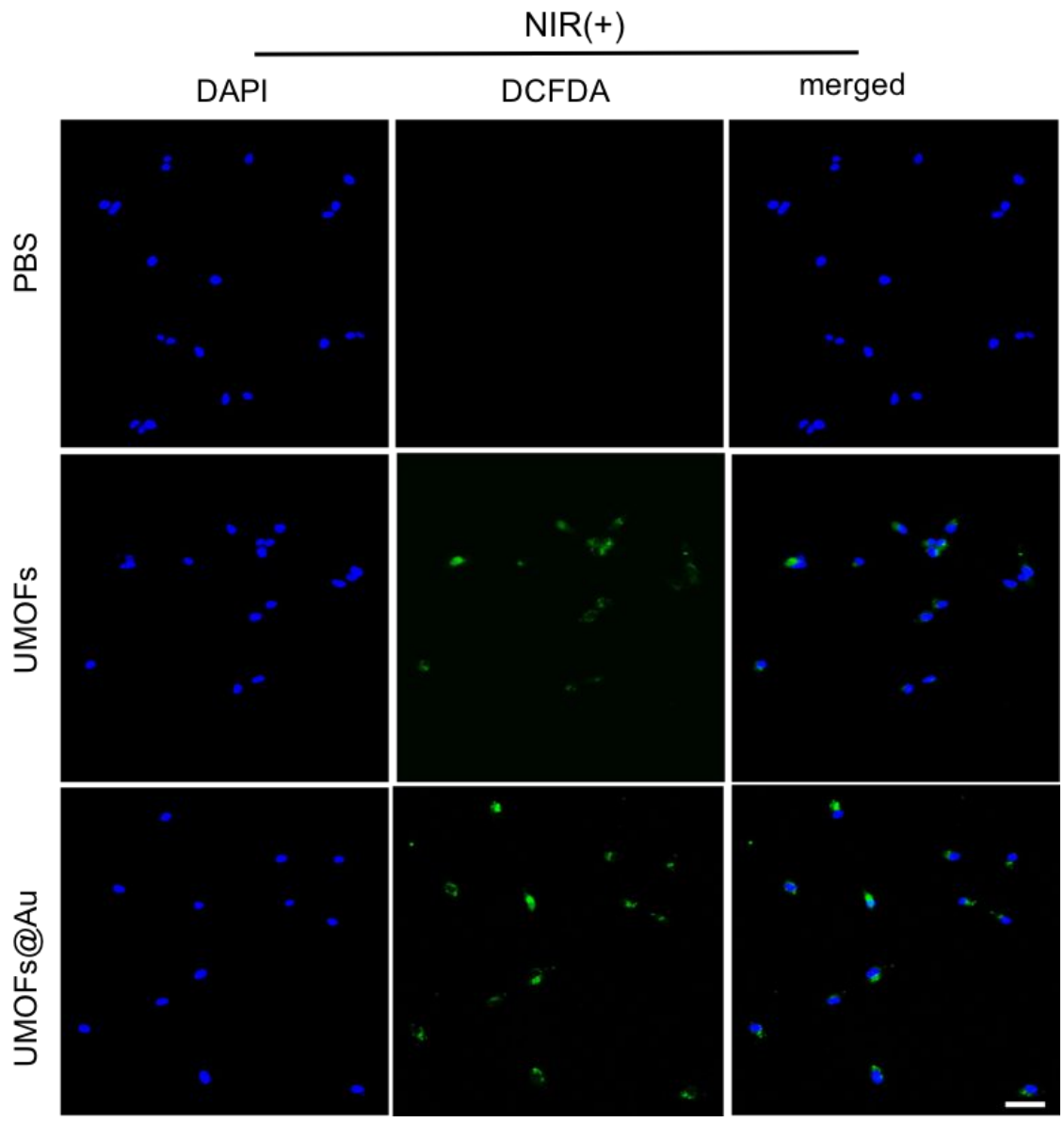

Figure S26. CLSM images of intracellular ROS generation by DCFDA assay. Six group experiments were conducted, with 980 nm laser irradiation.

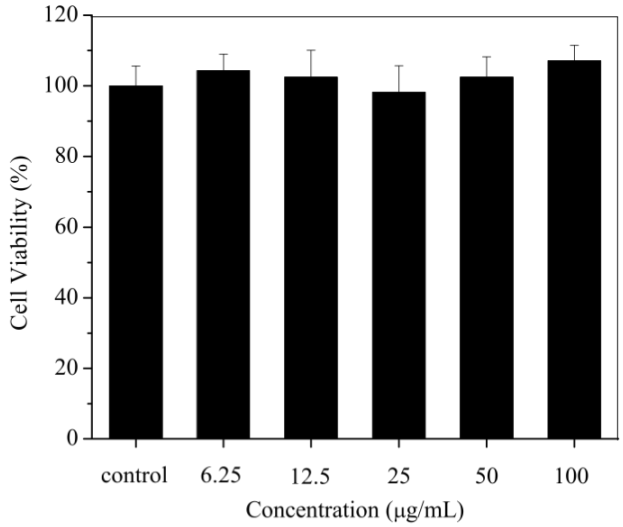

Figure S27. Cell viability of the U87MG cells treated with different concentrations of UMOFs NPs.

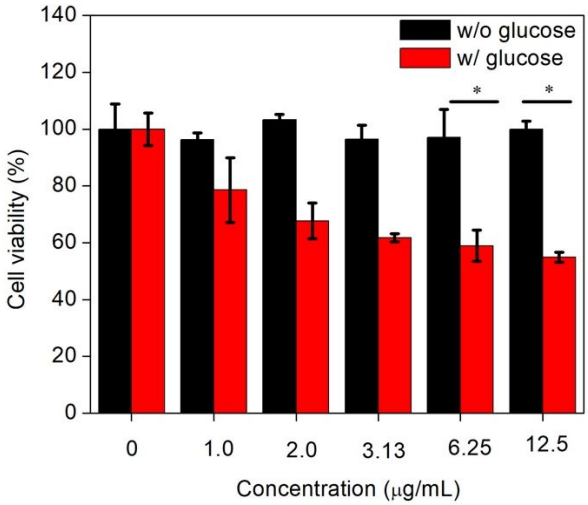

Figure S28. Cell viability of the U87MG cells treatment with different concentrations of UMOFs@Au NPs with and without glucose. * $P < 0.05$.

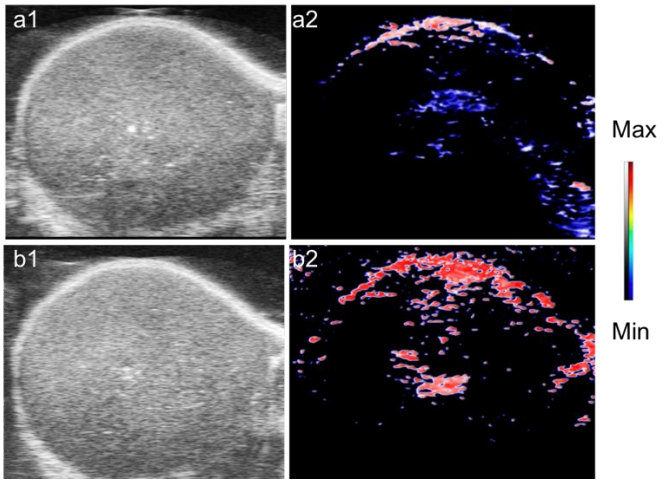

Figure S29. (a1, b1) *In vivo* evaluation of ultrasound imaging (US) at 0 h time point, (a2, b2) *In vivo* estimation of O_2 saturation of hemoglobin by photoacoustic (PA) imaging at 24 h time point. The mice were Intravenously injected with UMOFs@Au NPs.

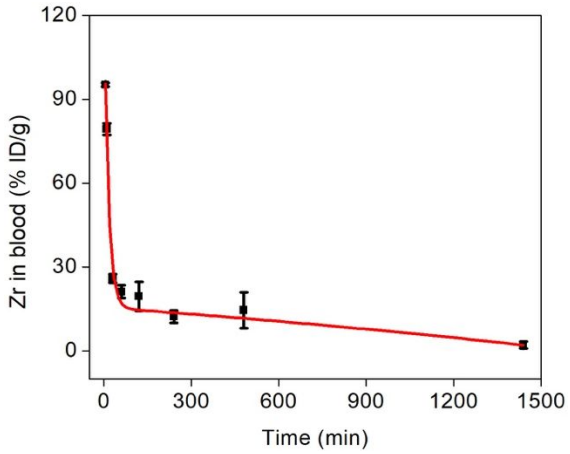

Figure S30. Blood circulation profile of UMOFs@Au NPs in mice after i.v. injection, as determined by ICP-measured Zr^{4+} concentrations in blood samples.

The blood circulation of UMOFs@Au was studied in U87MG tumor-bearing mice. The Zirconium concentrations in the blood of U87MG tumor-bearing mice after intravenous injection of UMOFs@Au were detected by ICP (n = 3, mean ± s.d). The blood was collected at 5 min, 10 min, 30 min, 1 h, 2 h, 4 h, 8 h and 24 h post-injection. According to the pharmacokinetic model, the blood terminal half-live of UMOFs@Au is calculated to be 78.2 min ($t_{1/2}$=0.693/k). C=112.88*exp(-x/14.61)-26.82*exp(x/3542.48) + 42.4.

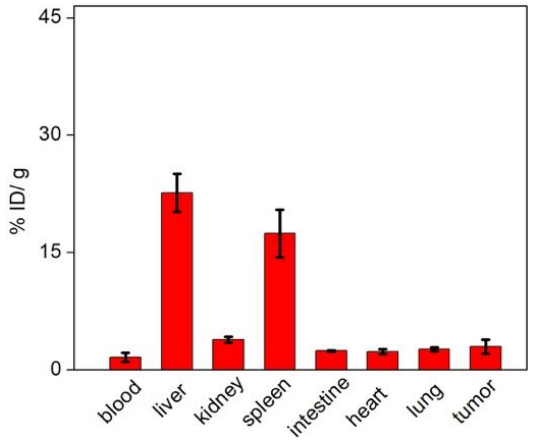

Figure S31. Biodistribution of ^{64}Cu-labeled UMOFs@Au by PET scan. The mice were injected with the ^{64}Cu-doped NPs (n = 3), and the primary tissues were collected at 48 h p.i. for region of interest analysis. *Ex vivo* biodistribution quantification was carried out at 48 h p.i. using a gamma counter, in which the results matched well with those quantified from PET images.

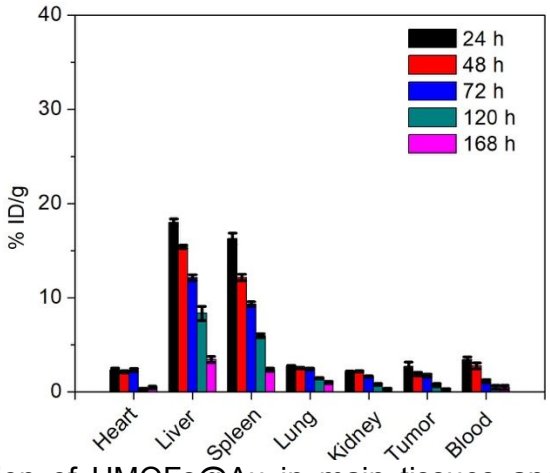

Figure S32. Biodistribution of UMOFs@Au in main tissues and tumor after intravenous administration for varied time intervals (24, 48, 72, 120, and 168 h) (n = 3). The UMOFs@Au concentrations were normalized as the percentage of the injected dose of Zr element (ID) per gram of each organ (% ID/g).

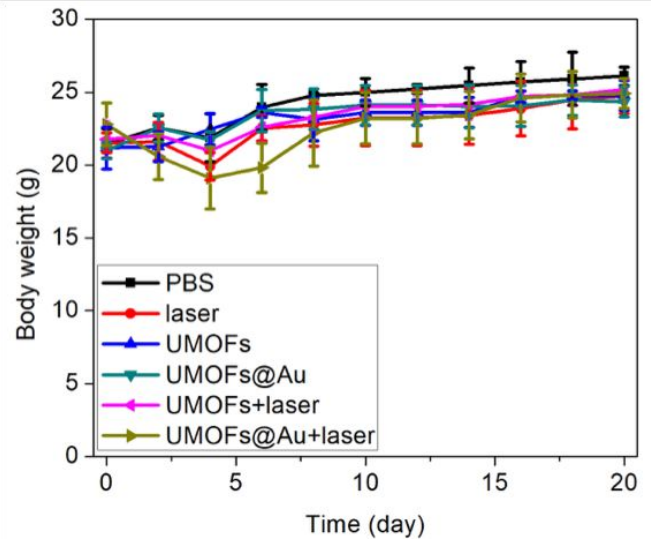

Figure S33. Body weight changes of the tumor bearing mice with various treatments.

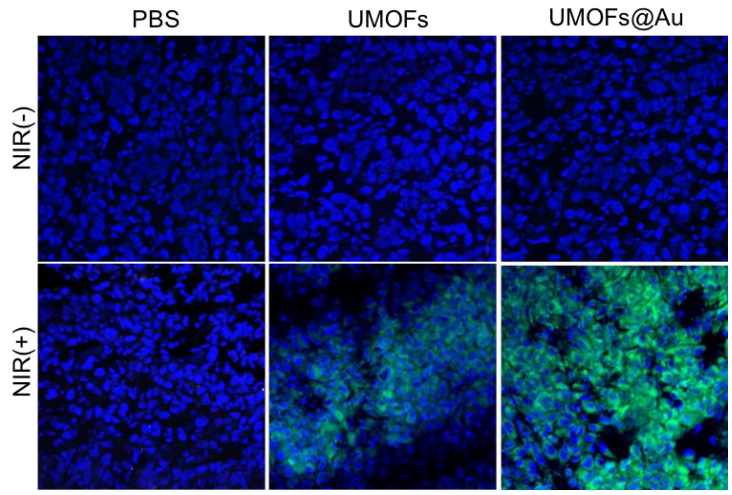

Figure S34. TUNEL assays on tumors subjected to different treatments. A significantly higher level of apoptotic cells was found in the synergistic UMOFs@Au NPs (with laser irradiation) treatment group.

Table S3. Summary of the important and related UCNPs-based PDT system.

Nanoparticle type	UCNPs type	UCNPs size (nm)	PDT (dose)	Laser power (W/cm^2)	Reference
dye-UCNPs	$NaYF_4$, Yb/Er-Ce_6	~30	*in vivo* PDT (800 μg/mice)	500 mW, 30 min; intratumoral injection	27
UCNPs@ SiO_2-ZnPc	$NaYF_4$: Yb,Er	~90	*in vivo* PDT	2.5, in vitro; 0.415 W/cm^2, 2 h; subcutaneous injection	28
core-shell	$NaYF_4$:Yb, Tm@ TiO_2	~50	*in vivo* PDT (650 μg/mice)	Total power: 500 mW, 33 min	29
UCNPs@ SiO_2	$NaYF_4$: Yb/Er/ Gd	~35	*in vivo* PDT (0.8 mg/mice)	1.4 W/cm^2	30
dye-UCNPs	$NaYF_4$: Yb/Er/Nd-Ce6	~40	*in vivo* PDT (3 mg/mice)	400 mW/cm^2, 45 min, intratumoral injection	13
core-satellite	$NaYF_4$, Yb/Er	23.8 ± 1.4	*in vitro* PDT (first work on porphyrin MOF-UCNPs for PDT)	15.9 W/cm^2	31
MOF-UCNPs dimer	$NaGdF_4$: Yb/Er @$NaGdF_4$	19 x 8	*in vivo* PDT+drug (40 mg/kg, 0.8 mg/mice)	1.2 W/cm^2	17
core-shell-shell@SiO_2	$NaGdF_4$@ $NaGdF_4$:Yb, Er@$NaGdF_4$	32	*in vivo* PDT (40 mg/kg, ~0.8 mg/mice)	1.0 W/cm^2 (808 laser) + 1.2 W/cm^2 (980) intratumoral injection	32
core-shell	$NaGdF_4$:Yb/ Tm@$NaGdF_4$ -CpG	~41	gene	1.2 W/cm^2 (tumor: 50 mm^3)	33
core-shell	$NaYF_4$, Yb/Er/Tm@ $NaYF_4$,Yb/Lu	~100	*in vivo* PDT+gene (50 mg/kg, ~1 mg/mice)	0.6 W/cm^2 (unknow, injection method)	34
MOF-UCNPs dimer	$NaGdF_4$:Yb, Er@$NaGdF_4$: Yb,Nd@ $NaGdF_4$	32	*in vivo* PDT (40 mg/kg)	1.0 W/cm^2 (808 laser)	35
core-shell (ultrasmall AuNPs decorated core-shell structures)	$NaYF_4$@ $NaYbF_4$:Er @$NaYF_4$	29.8 ± 2.2	cascaded reactions-driven PDT (*in vivo*) (0.3 mg/mice)	1.0 W/cm^2 laser spot size: ~2 mm in diameter Total power: ~125.6 mW	This work

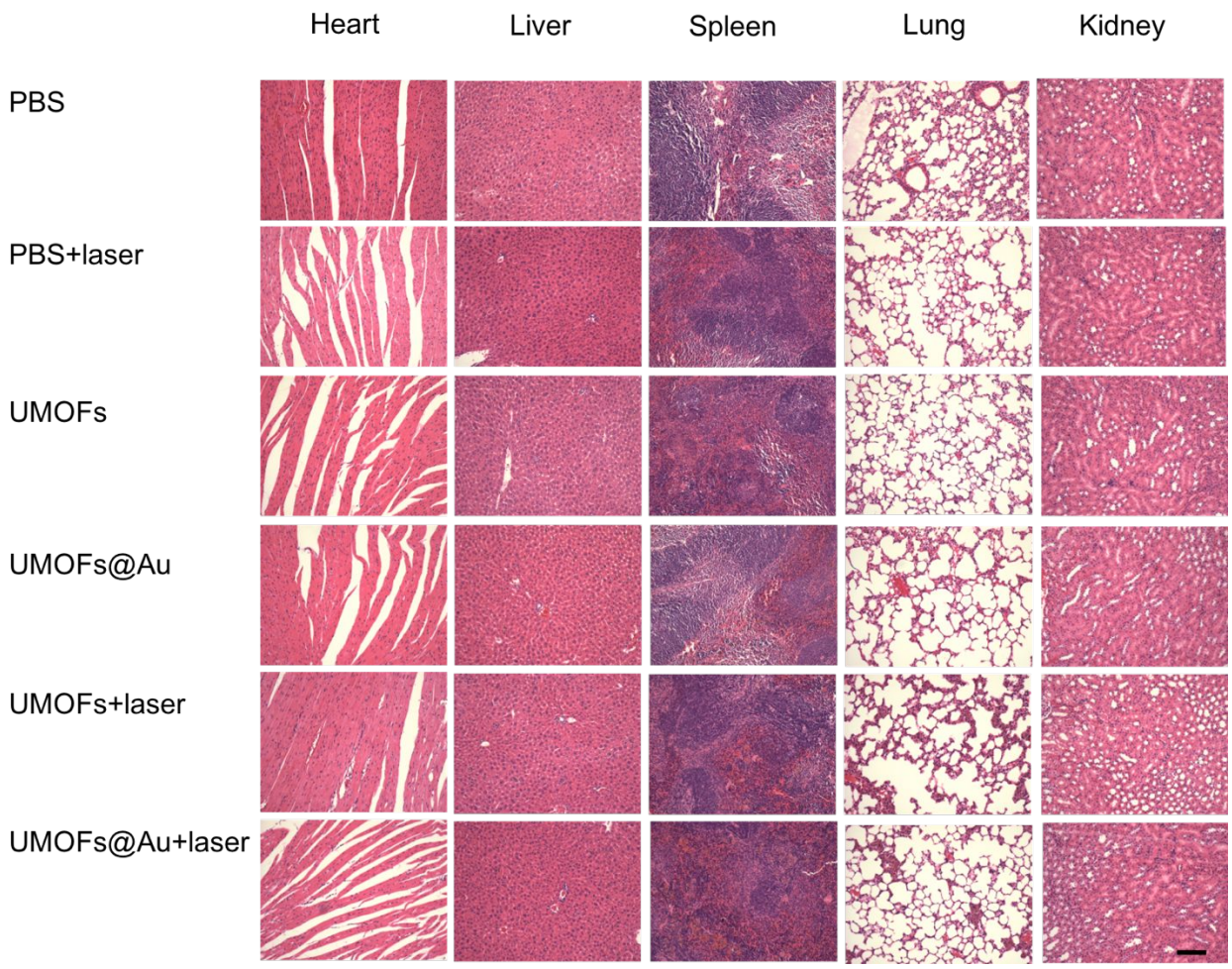

Figure S35. H&E staining on major organs (heart, liver, spleen, lung, and kidneys) at the end of the therapy studies. No obvious pathological abnormalities were observed. Scale bar, 100 μm.

Reference

(1) Boyer, J.-C.; van Veggel, F. C. J. M. Absolute quantum yield measurements of colloidal $NaYF_4$: Er^{3+}, Yb^{3+} upconverting nanoparticles. *Nanoscale* **2010,** *2* (8), 1417.

(2) Tian, J.; Ding, L.; Xu, H.-J.; Shen, Z.; Ju, H.; Jia, L.; Bao, L.; Yu, J.-S. Cell-Specific and pH-Activatable Rubyrin-Loaded Nanoparticles for Highly Selective Near-

Infrared Photodynamic Therapy against Cancer. *Journal of the American Chemical Society* **2013,** *135* (50), 18850.
(3) Zhang, L.; Lei, J.; Ma, F.; Ling, P.; Liu, J.; Ju, H. A porphyrin photosensitized metal-organic framework for cancer cell apoptosis and caspase responsive theranostics. *Chemical Communications* **2015,** *51* (54), 10831.
(4) Yue, Z.-G.; Wei, W.; You, Z.-X.; Yang, Q.-Z.; Yue, H.; Su, Z.-G.; Ma, G.-H. Iron Oxide Nanotubes for Magnetically Guided Delivery and pH-Activated Release of Insoluble Anticancer Drugs. *Advanced Functional Materials* **2011,** *21* (18), 3446.
(5) Wang, F.; He, S.; Wang, H.; Zhang, S.; Wu, C.; Huang, H.; Pang, Y.; Tsung, C.-K.; Li, T. Uncovering two kinetic factors in the controlled growth of topologically distinct core-shell metal-organic frameworks. *Chemical Science* **2019,** *10* (33), 7755.
(6) Yang, X.; Yuan, S.; Zou, L.; Drake, H.; Zhang, Y.; Qin, J.; Alsalme, A.; Zhou, H. C. One-Step Synthesis of Hybrid Core-Shell Metal-Organic Frameworks. *Angewandte Chemie International Edition* **2018,** *57* (15), 3927.
(7) Wang, F.; Wang, H.; Li, T. Seaming the interfaces between topologically distinct metal–organic frameworks using random copolymer glues. *Nanoscale* **2019,** *11* (5), 2121.
(8) Zhuang, J.; Chou, L.-Y.; Sneed, B. T.; Cao, Y.; Hu, P.; Feng, L.; Tsung, C.-K. Surfactant-Mediated Conformal Overgrowth of Core-Shell Metal-Organic Framework Materials with Mismatched Topologies. *Small* **2015,** *11* (41), 5551.
(9) Feng, L.; Wang, K.-Y.; Powell, J.; Zhou, H.-C. Controllable Synthesis of Metal-Organic Frameworks and Their Hierarchical Assemblies. *Matter* **2019,** *1* (4), 801.
(10) Zhao, Y.; Jiang, L.; Shangguan, L.; Mi, L.; Liu, A.; Liu, S. Synthesis of porphyrin-based two-dimensional metal-organic framework nanodisk with small size and few layers. *Journal of Materials Chemistry A* **2018,** *6* (6), 2828.
(11) Zou, W.; Visser, C.; Maduro, J. A.; Pshenichnikov, M. S.; Hummelen, J. C. Broadband dye-sensitized upconversion of near-infrared light. *Nat Photon* **2012,** *6* (8), 560.
(12) Liu, H.; Xu, C. T.; Lindgren, D.; Xie, H.; Thomas, D.; Gundlach, C.; Andersson-Engels, S. Balancing power density based quantum yield characterization of upconverting nanoparticles for arbitrary excitation intensities. *Nanoscale* **2013,** *5* (11), 4770.
(13) Ai, X.; Ho, C. J. H.; Aw, J.; Attia, A. B. E.; Mu, J.; Wang, Y.; Wang, X.; Wang, Y.; Liu, X.; Chen, H.et al. In vivo covalent cross-linking of photon-converted rare-earth nanostructures for tumour localization and theranostics. *Nat Commun* **2016,** *7*, 10432.
(14) Wu, X.; Zhang, Y.; Takle, K.; Bilsel, O.; Li, Z.; Lee, H.; Zhang, Z.; Li, D.; Fan, W.; Duan, C.et al. Dye-Sensitized Core/Active Shell Upconversion Nanoparticles for Optogenetics and Bioimaging Applications. *ACS Nano* **2016,** *10* (1), 1060.
(15) Zhang, Y.; Yu, Z.; Li, J.; Ao, Y.; Xue, J.; Zeng, Z.; Yang, X.; Tan, T. T. Y. Ultrasmall-Superbright Neodymium-Upconversion Nanoparticles via Energy Migration Manipulation and Lattice Modification: 808 nm-Activated Drug Release. *ACS Nano* **2017,** *11* (3), 2846.
(16) Chen, Q.; Xie, X.; Huang, B.; Liang, L.; Han, S.; Yi, Z.; Wang, Y.; Li, Y.; Fan, D.; Huang, L.et al. Confining Excitation Energy in Er3+-Sensitized Upconversion

Nanocrystals through Tm3+-Mediated Transient Energy Trapping. *Angewandte Chemie International Edition* **2017,** *56* (26), 7605.
(17) Li, Y.; Di, Z.; Gao, J.; Cheng, P.; Di, C.; Zhang, G.; Liu, B.; Shi, X.; Sun, L.-D.; Li, L.et al. Heterodimers Made of Upconversion Nanoparticles and Metal–Organic Frameworks. *Journal of the American Chemical Society* **2017,** *139* (39), 13804.
(18) Fernandez-Bravo, A.; Yao, K.; Barnard, E. S.; Borys, N. J.; Levy, E. S.; Tian, B.; Tajon, C. A.; Moretti, L.; Altoe, M. V.; Aloni, S.et al. Continuous-wave upconverting nanoparticle microlasers. *Nature Nanotechnology* **2018,** *13* (7), 572.
(19) Liu, Q.; Zhang, Y.; Peng, C. S.; Yang, T.; Joubert, L.-M.; Chu, S. Single upconversion nanoparticle imaging at sub-10 W cm^{-2} irradiance. *Nature Photonics* **2018,** *12*, 548.
(20) Wen, S.; Zhou, J.; Schuck, P. J.; Suh, Y. D.; Schmidt, T. W.; Jin, D. Future and challenges for hybrid upconversion nanosystems. *Nature Photonics* **2019,** *13* (12), 828.
(21) Chen, G.; Shao, W.; Valiev, R. R.; Ohulchanskyy, T. Y.; He, G. S.; Ågren, H.; Prasad, P. N. Efficient Broadband Upconversion of Near-Infrared Light in Dye-Sensitized Core/Shell Nanocrystals. *Advanced Optical Materials* **2016,** *4* (11), 1760.
(22) Yan, S.; Zeng, X.; Tang, Y. a.; Liu, B.-F.; Wang, Y.; Liu, X. Activating Antitumor Immunity and Antimetastatic Effect Through Polydopamine-Encapsulated Core-Shell Upconversion Nanoparticles. *Advanced Materials* **2019,** *31* (46), 1905825.
(23) Ma, Y.; Bao, J.; Zhang, Y.; Li, Z.; Zhou, X.; Wan, C.; Huang, L.; Zhao, Y.; Han, G.; Xue, T. Mammalian Near-Infrared Image Vision through Injectable and Self-Powered Retinal Nanoantennae. *Cell* **2019,** *177* (2), 243.
(24) Bao, G.; Jin, D. Nanoparticles give mice infrared vision. *Nature Photonics* **2019,** *13* (5), 304.
(25) Wisser, M. D.; Fischer, S.; Siefe, C.; Alivisatos, A. P.; Salleo, A.; Dionne, J. A. Improving Quantum Yield of Upconverting Nanoparticles in Aqueous Media via Emission Sensitization. *Nano Letters* **2018,** *18* (4), 2689.
(26) Huo, M.; Wang, L.; Chen, Y.; Shi, J. Tumor-selective catalytic nanomedicine by nanocatalyst delivery. *Nature Communications* **2017,** *8* (1), 357.
(27) Wang, C.; Tao, H.; Cheng, L.; Liu, Z. Near-infrared light induced in vivo photodynamic therapy of cancer based on upconversion nanoparticles. *Biomaterials* **2011,** *32* (26), 6145.
(28) Idris, N. M.; Gnanasammandhan, M. K.; Zhang, J.; Ho, P. C.; Mahendran, R.; Zhang, Y. In vivo photodynamic therapy using upconversion nanoparticles as remote-controlled nanotransducers. *Nature Medicine* **2012,** *18* (10), 1580.
(29) Lucky, S. S.; Muhammad Idris, N.; Li, Z.; Huang, K.; Soo, K. C.; Zhang, Y. Titania Coated Upconversion Nanoparticles for Near-Infrared Light Triggered Photodynamic Therapy. *ACS Nano* **2015,** *9* (1), 191.
(30) Liu, Y.; Liu, Y.; Bu, W.; Cheng, C.; Zuo, C.; Xiao, Q.; Sun, Y.; Ni, D.; Zhang, C.; Liu, J.et al. Hypoxia Induced by Upconversion-Based Photodynamic Therapy: Towards Highly Effective Synergistic Bioreductive Therapy in Tumors. *Angewandte Chemie International Edition* **2015,** *54* (28), 8105.
(31) He, L.; Brasino, M.; Mao, C.; Cho, S.; Park, W.; Goodwin, A. P.; Cha, J. N. DNA-Assembled Core-Satellite Upconverting-Metal-Organic Framework Nanoparticle

Superstructures for Efficient Photodynamic Therapy. *Small* **2017,** *13* (24), 1700504.
(32) Mi, Y.; Cheng, H.-B.; Chu, H.; Zhao, J.; Yu, M.; Gu, Z.; Zhao, Y.; Li, L. A photochromic upconversion nanoarchitecture: towards activatable bioimaging and dual NIR light-programmed singlet oxygen generation. *Chemical Science* **2019,** *10* (44), 10231.
(33) Chu, H.; Zhao, J.; Mi, Y.; Di, Z.; Li, L. NIR-light-mediated spatially selective triggering of anti-tumor immunity via upconversion nanoparticle-based immunodevices. *Nature Communications* **2019,** *10* (1), 2839.
(34) Zhang, Z.; Jayakumar, M. K. G.; Zheng, X.; Shikha, S.; Zhang, Y.; Bansal, A.; Poon, D. J. J.; Chu, P. L.; Yeo, E. L. L.; Chua, M. L. K.et al. Upconversion superballs for programmable photoactivation of therapeutics. *Nature Communications* **2019,** *10* (1), 4586.
(35) Liu, C.; Liu, B.; Zhao, J.; Di, Z.; Chen, D.; Gu, Z.; Li, L.; Zhao, Y. Nd^{3+}-Sensitized Upconversion Metal-Organic Frameworks for Mitochondria-Targeted Amplified Photodynamic Therapy. *Angewandte Chemie International Edition* **2020,** *59* (7), 2634.